Dual-arm Box Grabbing with Impact-aware MPC utilizing soft deformable End-effector Pads

Niels Dehio, Yuquan Wang, Abderrahmane Kheddar

Dual-arm Box Grabbing with Impact-aware MPC utilizing soft deformable End-effector Pads

Niels Dehio[1], Yuquan Wang[1], and Abderrahmane Kheddar[1,2], *Fellow, IEEE*

***Abstract*—Safely generating impacts is challenging due to subsequent discontinuous velocity jumps and high impact forces. For this reason, state-of-the-art multi-robot controllers performing collaborative object manipulation typically approach contacts with low relative velocities. We instead aim for high-speed bi-manual impact-aware swift grabbing tasks, generating intentionally maximum feasible impacts. Therefore, we propose that the robot end-effector tips be equipped with deformable soft pads. The hardware modification partially absorbs the shock and enables us to control the deformation state during the prolonged impact duration. Mapping the robot's structural hardware constraints from the high-dimensional configuration-space to the low-dimensional contact-space enables us to model the bounded deformation dynamics explicitly. Exploiting constrained model-predictive control (MPC), we maximize the impact velocity within the feasible limits for dual-arm setups with deformable end-effector tips. Our control paradigm is assessed with real-robot experiments on two redundant Panda manipulators, demonstrating high pre-impact velocities for boxes with varying weights and size. The approach also applies to grabbing soft objects with rigid end-effectors.**

***Index Terms*—Dual Arm Manipulation, Contact Modeling.**

I. Introduction

WE aim at enabling robotic fast grabbing and tossing of bulky box objects in automated industrial sorting chains[1]. Collaborative dual-arm manipulation – and more generally, multi-arm manipulation – has a long history in robotic research, dating back to the late 1980s with early works reported in [1], [2]. Bi-manual object manipulation allows us to overcome the payload limit of a single manipulator [3] and is a by-design choice for humanoid robots when lifting heavy weights [4], [5]. Classical research topics comprise optimization of contact locations and contact forces, manipulability optimization, identification of object dynamics, and many more. However, few studied high-speed contact transitions for swiftly grabbing rigid objects bi-manually.

We want to maximize feasible end-effector velocities for the contact grabbing, prior to lifting, inherent in bi-manual tasks without damaging the robot arms and the grabbed objects. This is a non-trivial challenge w.r.t the maximum impact that gearboxes and torque sensors can handle.

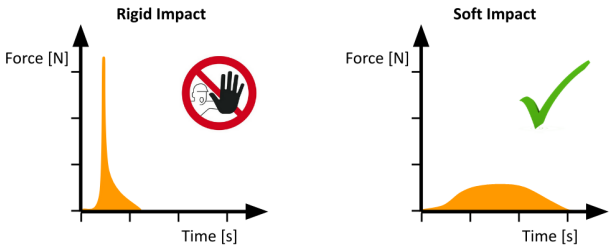

Fig. 1: Schematic illustration of impact forces for a given mass and pre-impact velocity with a rigid (left) and soft (right) contacts.

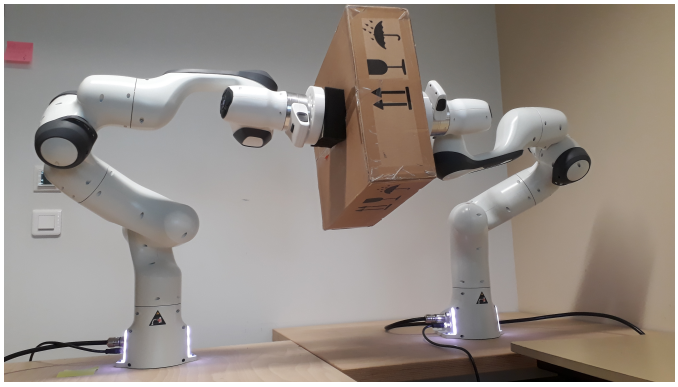

Fig. 2: Two Panda manipulators with soft, deformable pads attached to the end-effectors. We initiate contacts for swift box grabbing with pre-impact velocities of 0.61 m/s. The video is available at: https://youtu.be/dPLNfl7knF8

We propose utilizing soft, deformable end-effector pads for dual-arm grabbing tasks. The softness will absorb a large part of the kinetic energy, allowing for higher impact velocities compared to rigid end-effectors. Figure 1 illustrates the shape of the contact force at impact: the same mass and contact velocity leads to a significant force peak in the rigid case, whereas in a soft case the force curve is flattened. Consequently, a soft pad at end-effectors increases the set of physically possible robot movements when it comes to contact with rigid objects. Yet, trajectory planning and control requires material's softness modeling in order to fully exploit deformable end-effector pads.

Our main contribution is the derivation of *bounded deformation dynamics* for a dual-arm system with deformable end-effector pads. These constrained deformation dynamics provide the basis for a model predictive control (MPC) scheme [6], [7], [8], generalized from single-arm poking [9]

Manuscript received September 29, 2021; Revised January 16, 2022; Accepted February 21, 2022.

This paper was recommended for publication by Editor Markus Vincze upon evaluation of the Associate Editor and Reviewers' comments. This work is in part supported by the Research Project I.AM. through the European Union H2020 program (GA 871899).

[1] N. Dehio, Y. Wang and A. Kheddar are with the CNRS-University of Montpellier LIRMM Interactive Digital Humans group, Montpellier, France. niels.dehio,yuquan.wang,kheddar@lirmm.fr

[2] A. Kheddar is also with the CNRS-AIST Joint Robotics Laboratory, IRL, Tsukuba, Japan.

Digital Object Identifier (DOI): see top of this page.

[1]Refer to **I**mpact-**A**ware **M**anipulation https://i-am-project.eu

to dual-arm grabbing. The MPC optimizes the deformation trajectory, which is to be initiated with the highest possible end-effector velocities. Our formulation maps structural hardware limits of two potentially redundant robot arms[2] onto the low-dimensional contact-space. Including these inequality constraints into the deformation dynamics ensures safe operation over a sufficiently long preview-horizon. Compared to existing works, the novelty of our approach lies in the explicit computation of the maximum feasible contact velocity for a dual-arm robot setup to swiftly grab a rigid object bi-manually.

We assessed our impact-aware controller with various objects grabbing experiments with two Panda manipulators, see Fig. 2 and shown in the accompanying video available at https://youtu.be/dPLNfl7knF8. We could successfully achieve high impact velocities without violating hardware limitations. Executing the rigid box grabbing task without soft pads and similar (to soft) contact velocities would trigger the robot's safety reflex, resulting in a freeze-stop and potential hardware damage. On the other hand, our approach also applies to grabbing known soft objects with rigid end-effectors.

II. Related Works

It is difficult to predict accurately contact forces (in this case, impulses) or stress induced from two-impacting bodies [10]. Conventional contact mechanics, e.g., the Hertz theory, predict contact forces for spherical contact surfaces [11]. So far, the latter is limited to non-articulated objects and is not applicable for actuated robots with complex kinematic chains. This explains, in part, that related works on collaborative multi-arm robots establish contacts with relatively low end-effector velocities to grab objects [12], [13], [14].

Our pilot experiments confirm that an impact with a soft material significantly reduces the peak impulsive force and increases the overall impact duration, see the schematic illustration in Fig. 1. The approach for joint object manipulation in [3] uses deformable rubber elements attached on top of the rigid end-effector to mitigate the risk inherent to high peak impacts. Yet, the material softness and the actual deformations were not considered within the model-based torque-controller. Few works focused on modeling deformable robotic fingertips [15] and virtual spring-damper systems [16] for grasping scenarios, though, without discussing the resulting contact transitions. Contact forces arising from penetrating soft material have been precisely modeled in [17]. In [18] a deformable end-effector tip is modeled at the quasi-static level neglecting dynamic effects. The finite element method (FEM) is usually used in various continuum mechanics problems. It has been adopted in robotics to simulate material deformations, e.g., [19], [20], [21]; so far not in high-speed contact transitions with actuated robots.

The robot's structural hardware limits defined in the joint-space implicitly result in bounds in the contact-space. These bounds need to be fulfilled when intentionally generating impacts. Besides switching joint-space reference trajectories, where such limits are accounted in the off-line planned trajectories [22], to our best knowledge, only a few related works on task-space impact-aware control take these hardware limits into account. The prediction of impact-induced state jumps caused by rigid contacts is formulated in [23] to limit the end-effector speed prior to making contact. For impacting soft contacts with a manipulator, we inferred in [9] the configuration-dependent maximum feasible impact velocity. This upper velocity bound can be tracked with the robot arm before making contact, guaranteeing the robot's hardware limits during the following deformation phase.

An initial attempt towards impact-aware multi-arm box grabbing has been made in [24] with a humanoid and rigid contacts, lifting a lightweight, empty box. However, we are not aware of any study on swift dual-arm grabbing employing deformable material. In this paper, we explicitly model soft pads attached to two end-effectors in a dual-arm setup and devise a constrained impact-aware MPC in the contact-space, thereby extending and enhancing previous works.

III. Mapping Hardware Limits to Contact-Space

Let us elaborate further the mapping of the manipulator's structural hardware limits onto the contact-space, initially described in [9] and inspired by [25], [26]. This configuration-dependent mapping is not trivial when dealing with redundant robots. Considering the full Cartesian contact-space, the mapping procedure is computationally demanding and hence unsuitable for real-time control. Fortunately, the mapping simplifies, and a real-time solution exists when restricting the end-effector motion along the contact normal.

A. Constrained Robot State

Let us model the rigid-body dynamics for a fixed-base manipulator with N actuated joints in contact situation by

$$\boldsymbol{\tau} + \mathbf{J}_1^T \mathbf{f} = \mathbf{M}\ddot{\mathbf{q}} + \mathbf{h} \,, \tag{1}$$

where $\boldsymbol{\tau} \in \mathbb{R}^N$ are the joint torques, $\mathbf{f} \in \mathbb{R}$ is the scalar force along the contact normal, $\mathbf{M} \in \mathbb{R}^{N\times N}$ denotes the joint-space inertia, $\ddot{\mathbf{q}} \in \mathbb{R}^N$ are the joint accelerations, and $\mathbf{h} \in \mathbb{R}^N$ comprises gravity, Coriolis and centrifugal forces. The end-effector Jacobian $\mathbf{J} \in \mathbb{R}^{6\times N}$ consisting of six rows is decomposed as $\mathbf{J}_1 = \mathbf{o}_1^T\mathbf{J}$ and $\mathbf{J}_{2..6} = \mathbf{o}_{2..6}^T\mathbf{J}$ with the orthonormal base $\mathbf{O} = [\mathbf{o}_1, \mathbf{o}_{2..6}] \in \mathbb{R}^{6\times 6}$ and the vector $\mathbf{o}_1 \in \mathbb{R}^6$ corresponding to the contact normal. We assume a full-rank Jacobian $\mathbf{J}$ in this letter.

We represent the robot state (generalized coordinates) by the vector $\left[\mathbf{q}^T, \dot{\mathbf{q}}^T, \ddot{\mathbf{q}}^T, \mathbf{f}^T\right]^T \in \mathbb{R}^{3N+1}$, which implicitly includes the joint torques $\boldsymbol{\tau}$ through (1). The robot state is feasible at a given time instance when satisfying the structural hardware limits provided by the robot manufacturer[3]. These limits form a convex, high-dimensional polytope

$$\begin{bmatrix} \underline{\mathbf{q}} \\ \underline{\dot{\mathbf{q}}} \\ \underline{\ddot{\mathbf{q}}} \\ \underline{\mathbf{f}} \\ \underline{\boldsymbol{\tau}} - \mathbf{h} \end{bmatrix} \leq \begin{bmatrix} \mathbf{I}, & \mathbf{0}, & \mathbf{0}, & \mathbf{0} \\ \mathbf{0}, & \mathbf{I}, & \mathbf{0}, & \mathbf{0} \\ \mathbf{0}, & \mathbf{0}, & \mathbf{I}, & \mathbf{0} \\ \mathbf{0}, & \mathbf{0}, & \mathbf{0}, & \mathbf{I} \\ \mathbf{0}, & \mathbf{0}, & \mathbf{M}, & -\mathbf{J}_1^T \end{bmatrix} \begin{bmatrix} \mathbf{q} \\ \dot{\mathbf{q}} \\ \ddot{\mathbf{q}} \\ \mathbf{f} \end{bmatrix} \leq \begin{bmatrix} \bar{\mathbf{q}} \\ \bar{\dot{\mathbf{q}}} \\ \bar{\ddot{\mathbf{q}}} \\ \bar{\mathbf{f}} \\ \bar{\boldsymbol{\tau}} - \mathbf{h} \end{bmatrix} , \tag{2}$$

[2]The dual-arm system may be composed of redundant manipulators with different kinematic / dynamic properties from two different manufacturers.

[3]For example, find the limits for the Panda manipulator from FrankaEmika: https://frankaemika.github.io/docs/control_parameters.html#constants

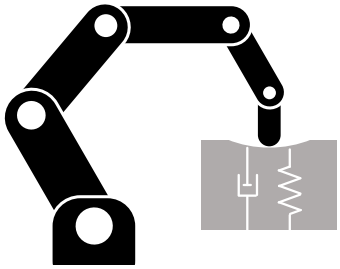

Fig. 3: A manipulator penetrating a deformable contact. The deformation velocity, acceleration, and force are bounded and depend on the particular robotic hardware limits.

where symbols $\underline{\star}$, $\bar{\star}$ denote lower and upper limits of $\star$, respectively. The particular hardware limits relate to the resilience of gearboxes and torque sensors, and to the maximum force a wrist-mounted force-torque sensor can afford. When planning a discretized robot trajectory, the robot state must fulfill (2) at each time instance.

In the following, we focus on an established contact situation with a deformable material, as indicated in Fig. 3. It is irrelevant for the analysis if the soft material is part of the environment or the robot. The scalar contact-space velocity $\dot{\mathbf{z}} = \mathbf{J}_1\dot{\mathbf{q}} \in \mathbb{R}$ and acceleration $\ddot{\mathbf{z}} = \mathbf{J}_1\ddot{\mathbf{q}} + \dot{\mathbf{J}}_1\dot{\mathbf{q}} \in \mathbb{R}$ in contact normal direction are generally non-zero. Besides, let us enforce zero end-effector velocity $\mathbf{0} = \dot{\mathbf{x}} = \mathbf{J}_{2..6}\dot{\mathbf{q}} \in \mathbb{R}^5$ and zero acceleration $\mathbf{0} = \ddot{\mathbf{x}} = \mathbf{J}_{2..6}\ddot{\mathbf{q}} + \dot{\mathbf{J}}_{2..6}\dot{\mathbf{q}} \in \mathbb{R}^5$ (i.e., no tangential contact velocity). These relationships are gathered in matrix form as

$$\begin{bmatrix} \mathbf{J}_1, & \mathbf{0}, & -\mathbf{I}, & \mathbf{0} \\ \mathbf{J}_{2..6}, & \mathbf{0}, & \mathbf{0}, & \mathbf{0} \\ \dot{\mathbf{J}}_1, & \mathbf{J}_1, & \mathbf{0}, & -\mathbf{I} \\ \dot{\mathbf{J}}_{2..6}, & \mathbf{J}_{2..6}, & \mathbf{0}, & \mathbf{0} \end{bmatrix} \begin{bmatrix} \dot{\mathbf{q}} \\ \ddot{\mathbf{q}} \\ \dot{\mathbf{z}} \\ \ddot{\mathbf{z}} \end{bmatrix} = \begin{bmatrix} \mathbf{0} \\ \mathbf{0} \\ \mathbf{0} \\ \mathbf{0} \end{bmatrix}, \tag{3}$$

To represent motion in the contact-space (along the contact normal), we define the low-dimensional deformation state $\left[\mathbf{z}^T, \dot{\mathbf{z}}^T, \ddot{\mathbf{z}}^T, \mathbf{f}^T\right]^T \in \mathbb{R}^4$, which is implicitly bounded by the hardware limits described above. The configuration-dependent contact-space bounds are explicitly derived in the following subsections by combining (2) and (3). In other words, we map the high-dimensional polytope onto the low-dimensional space, see also [27].

B. Contact-Space Bounds on Velocity

The lower bound on the contact-space velocity $\dot{\mathbf{z}}$ yields

$$\begin{aligned} \underline{\dot{\mathbf{z}}} = \min_{\dot{\mathbf{q}}} \quad & \mathbf{J}_1\dot{\mathbf{q}} \\ \text{s. t.} \quad & \mathbf{J}_{2..6}\,\dot{\mathbf{q}} = \mathbf{0} \\ & \underline{\dot{\mathbf{q}}} \le \dot{\mathbf{q}} \le \bar{\dot{\mathbf{q}}} \end{aligned} \tag{4}$$

due to the block-structure in (2) and (3). The upper velocity bound $\bar{\dot{\mathbf{z}}}$ is obtained by negating the objective function.

C. Contact-Space Bounds on Acceleration and Force

Due to the structure of (2), the bounds on contact-space acceleration $\ddot{\mathbf{z}}$ and force $\mathbf{f}$ are coupled and cannot be treated separately. Geometrically, the set of feasible $\ddot{\mathbf{z}}$ and $\mathbf{f}$ is represented by a two-dimensional convex polytope (= polygon). Its convex hull consists of multiple vertices. Such a vertex can be obtained by solving the linear program (for $\dot{\mathbf{J}}\dot{\mathbf{q}} \simeq \mathbf{0}$, refer to the explanation in Sec. IV-A)

$$\begin{aligned} \underset{\ddot{\mathbf{q}},\mathbf{f},\ddot{\mathbf{z}}}{\arg\min} \quad & \ddot{\mathbf{z}}\,\mathbf{v}_1 + \mathbf{f}\,\mathbf{v}_2 \\ \text{s. t.} \quad & \begin{bmatrix} \mathbf{J}_1, & \mathbf{0}, & -\mathbf{I} \\ \mathbf{J}_{2..6}, & \mathbf{0}, & \mathbf{0} \end{bmatrix} \begin{bmatrix} \ddot{\mathbf{q}} \\ \mathbf{f} \\ \ddot{\mathbf{z}} \end{bmatrix} = \begin{bmatrix} \mathbf{0} \\ \mathbf{0} \end{bmatrix} \\ & \begin{bmatrix} \underline{\ddot{\mathbf{q}}} \\ \underline{\mathbf{f}} \\ \underline{\boldsymbol{\tau}} - \mathbf{h} \end{bmatrix} \le \begin{bmatrix} \mathbf{I}, & \mathbf{0}, & \mathbf{0} \\ \mathbf{0}, & \mathbf{I}, & \mathbf{0} \\ \mathbf{M}, & -\mathbf{J}_1^T, & \mathbf{0} \end{bmatrix} \begin{bmatrix} \ddot{\mathbf{q}} \\ \mathbf{f} \\ \ddot{\mathbf{z}} \end{bmatrix} \le \begin{bmatrix} \bar{\ddot{\mathbf{q}}} \\ \bar{\mathbf{f}} \\ \bar{\boldsymbol{\tau}} - \mathbf{h} \end{bmatrix} \end{aligned} \tag{5}$$

The scalar weights $\mathbf{v}_1, \mathbf{v}_2 \in \mathbb{R}$ can be geometrically interpreted as a two-dimensional ray pointing in a particular search direction. By solving (5) multiple times for different rays, a list of vertices is collected, approximating the convex hull of feasible $\ddot{\mathbf{z}}$ and $\mathbf{f}$. Refer to [27] and [28] for an efficient algorithm to select meaningful search directions (rays), such that the convex hull is well covered after few iterations. The vertex representation is converted into an equivalent half-space representation, where matrix $\mathbf{P} = [\mathbf{P}_{\ddot{\mathbf{z}}}, \mathbf{P}_{\mathbf{f}}]$ determines halfplanes, and vectors $\underline{\mathbf{p}}, \bar{\mathbf{p}}$ denote offsets

$$\underline{\mathbf{p}} \le \mathbf{P}_{\ddot{\mathbf{z}}}\ddot{\mathbf{z}} + \mathbf{P}_{\mathbf{f}}\mathbf{f} \le \bar{\mathbf{p}}\,. \tag{6}$$

D. Contact-Space Bounds on Deformation Position

We assume an unilateral contact, implying that the soft material cannot be stretched by pulling. Further, the material has a maximum penetration depth depending on its thickness and the elastic deformation domain. Hence, the scalar contact deformation $\mathbf{z} \in \mathbb{R}$ (related to the initial contact point and the absolute end-effector position along the contact normal) satisfies lower and upper bounds $\underline{\mathbf{z}}, \bar{\mathbf{z}}$ to be within the deformation domain.

E. Constrained Deformation State

Summarizing the previous derivation, the low-dimensional deformation state $\left[\mathbf{z}^T, \dot{\mathbf{z}}^T, \ddot{\mathbf{z}}^T, \mathbf{f}^T\right]^T$ is feasible at a given time instance when satisfying the bounds

$$\begin{bmatrix} \underline{\mathbf{z}} \\ \underline{\dot{\mathbf{z}}} \\ \underline{\mathbf{p}} \end{bmatrix} \le \begin{bmatrix} \mathbf{I}, & \mathbf{0}, & \mathbf{0}, & \mathbf{0} \\ \mathbf{0}, & \mathbf{I}, & \mathbf{0}, & \mathbf{0} \\ \mathbf{0}, & \mathbf{0}, & \mathbf{P}_{\ddot{\mathbf{z}}}, & \mathbf{P}_{\mathbf{f}} \end{bmatrix} \begin{bmatrix} \mathbf{z} \\ \dot{\mathbf{z}} \\ \ddot{\mathbf{z}} \\ \mathbf{f} \end{bmatrix} \le \begin{bmatrix} \bar{\mathbf{z}} \\ \bar{\dot{\mathbf{z}}} \\ \bar{\mathbf{p}} \end{bmatrix}. \tag{7}$$

It is important to note that a feasible deformation state also guarantees the existence of an associated feasible robot state $\left[\mathbf{q}^T, \dot{\mathbf{q}}^T, \ddot{\mathbf{q}}^T, \mathbf{f}^T\right]^T$. When planning a discretized deformation trajectory, the deformation state must achieve (7) at each time instance.

F. Illustrative Example

Consider a planar manipulator with two rotational joints. The link lengths are $l_1 = 0.5$ m, $l_2 = 0.3$ m, link masses are $m_1 = 3$ kg, $m_2 = 2$ kg, and the center-of-mass is located in each link center. The upper hardware limits are given by $\bar{\dot{\mathbf{q}}} = [2, 3]^T$ rad/s, $\bar{\ddot{\mathbf{q}}} = [10, 20]^T$ rad/s^2, $\bar{\boldsymbol{\tau}} = [25, 10]^T$ Nm, $\bar{\mathbf{f}} = 100$ N, and the lower limits are their negative values.

Let us analyze the specific posture $\mathbf{q} = [\pi/3, -\pi/3]$ rad, assuming the end-effector established a soft, deformable contact. The end-effector is pointing along the vector $[1, 0]^T$, also treated as the contact normal. Given (2) and (3), we extract the individual constraints w.r.t. velocities

$$\underline{\dot{\mathbf{q}}} \leq \dot{\mathbf{q}} \leq \bar{\dot{\mathbf{q}}}\,, \tag{7a}$$
$$\dot{\mathbf{z}} = \mathbf{J}_1\dot{\mathbf{q}}\,, \tag{7b}$$
$$\dot{\mathbf{x}} = \mathbf{J}_2\dot{\mathbf{q}}\,, \tag{7c}$$
$$\mathbf{0} = \dot{\mathbf{x}} = \mathbf{J}_2\dot{\mathbf{q}}\,, \tag{7d}$$

and w.r.t. the coupled acceleration and force

$$\underline{\ddot{\mathbf{q}}} \leq \ddot{\mathbf{q}} \leq \bar{\ddot{\mathbf{q}}}\,, \tag{7e}$$
$$\underline{\mathbf{f}} \leq \mathbf{f} \leq \bar{\mathbf{f}}\,, \tag{7f}$$
$$\underline{\boldsymbol{\tau}} - \mathbf{h} \leq \mathbf{M}\ddot{\mathbf{q}} - \mathbf{J}_1^T\mathbf{f} \leq \bar{\boldsymbol{\tau}} - \mathbf{h}\,, \tag{7g}$$
$$\ddot{\mathbf{z}} = \mathbf{J}_1\ddot{\mathbf{q}} + \dot{\mathbf{J}}_1\dot{\mathbf{q}}\,, \tag{7h}$$
$$\ddot{\mathbf{x}} = \mathbf{J}_2\ddot{\mathbf{q}} + \dot{\mathbf{J}}_2\dot{\mathbf{q}}\,, \tag{7i}$$
$$\mathbf{0} = \ddot{\mathbf{x}} = \mathbf{J}_2\ddot{\mathbf{q}} + \dot{\mathbf{J}}_2\dot{\mathbf{q}}\,. \tag{7j}$$

The blue 2D-polytopes (i.e., polygons) in Fig. 4 show the feasible set in terms of joint velocities $\dot{\mathbf{q}}_1, \dot{\mathbf{q}}_2$ (top part)

$$\mathcal{X}_1 = \left\{\dot{\mathbf{q}} \in \mathbb{R}^2 \middle|\, (7a)\right\}, \text{ and} \tag{8a}$$

its mapping onto end-effector velocities $\dot{\mathbf{z}}, \dot{\mathbf{x}}$ (bottom part)

$$\mathcal{X}_2 = \left\{\dot{\mathbf{z}} \in \mathbb{R}, \dot{\mathbf{x}} \in \mathbb{R}, \dot{\mathbf{q}} \in \mathbb{R}^2 \middle|\, (7a) - (7c)\right\}. \tag{8b}$$

The red 1D-polytope (line segment with scalar upper/lower bounds) indicates how these feasible sets shrink when additionally enforcing (7d) to avoid a tangential contact velocity.

Figure 5 highlights the coupling between acceleration and force. The four sub-figures from top to bottom show the four 3D-polytopes $\mathcal{Y}_1$, $\mathcal{Y}_2$, $\mathcal{Y}_3$, $\mathcal{Y}_4$ utilizing a triangularization technique for visualization, where the last one ($\mathcal{Y}_4$) shrinks to 2D due to additionally enforcing (7j)

$$\mathcal{Y}_1 = \left\{\ddot{\mathbf{q}} \in \mathbb{R}^2, \mathbf{f} \in \mathbb{R} \middle|\, (7e) - (7f)\right\}, \tag{8a}$$
$$\mathcal{Y}_2 = \left\{\ddot{\mathbf{q}} \in \mathbb{R}^2, \mathbf{f} \in \mathbb{R} \middle|\, (7e) - (7g)\right\}, \tag{8b}$$
$$\mathcal{Y}_3 = \left\{\ddot{\mathbf{z}} \in \mathbb{R}, \ddot{\mathbf{x}} \in \mathbb{R}, \ddot{\mathbf{q}} \in \mathbb{R}^2, \mathbf{f} \in \mathbb{R} \middle|\, (7e) - (7i)\right\}, \tag{8c}$$
$$\mathcal{Y}_4 = \left\{\ddot{\mathbf{z}} \in \mathbb{R}, \ddot{\mathbf{x}} \in \mathbb{R}, \ddot{\mathbf{q}} \in \mathbb{R}^2, \mathbf{f} \in \mathbb{R} \middle|\, (7e) - (7j)\right\}. \tag{8d}$$

IV. Approach

Our proposed impact-aware dual-arm grabbing controller is provided, as input, with the preferred contacting points for each category of objects. These pair of contact points are collinear line to opposite contact normal directions and parallel tangent to contact normal planes. Because we aim at swiftly grabbing (not grasping) and conformably with industrial recommendations, contacts on objects are chosen so as to not generate rotational torque during the grabbing phase. There is no restriction on their shape; a deforming pad allows casting locally the object's surface at the contacting spots.

While approaching the object to be grabbed with two soft end-effectors, in each cycle, the controller expects that both contact events will happen in the next iteration. With this expectation, the controller repeatedly recomputes and tracks

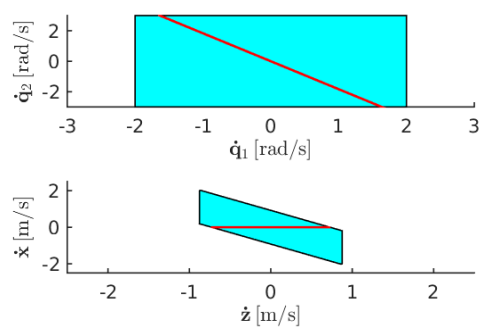

Fig. 4: Top: feasible set (8a). Bottom: (8b).

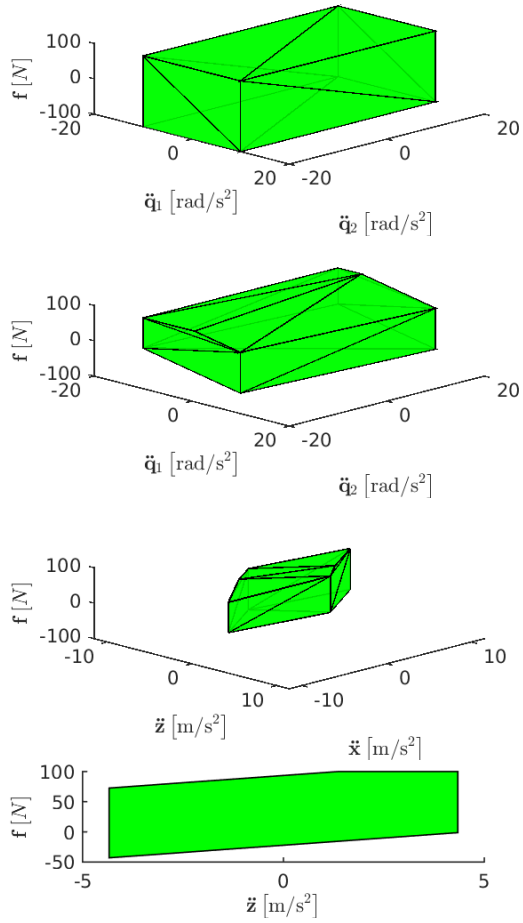

Fig. 5: Top to bottom: feasible sets (8a)-(8d).

the maximum feasible (configuration-dependent) pre-impact velocities. By doing so, the controller is robust to object's width uncertainties and to exact contact timing and localization (along the normal). Our approach generates intentional impacts for swift dual-arm grabbing without violating hardware limits during the deformation phase.

In the following, we derive a bounded deformation dynamics model; formulate a constrained optimization problem for planning and controlling a feasible dual-arm penetration trajectory; explain how our controller handles light asynchronous contact events; and provide a comparison to our previous work on impact-aware single-arm soft poking.

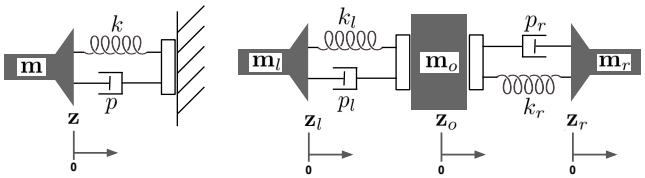

Fig. 6: Left: Soft pad modeled as a mass-spring-damper system attached to the end-effector. Right: Bi-manually grasping a rigid object with soft pads attached to both end-effectors. Important parameters are stiffness k, damping p, and effective mass $\mathbf{m}$. The deformation position is $\mathbf{z}$.

A. Bounded Dual-Arm Deformation Dynamics

In [9], we proposed the bounded deformation dynamics model for poking soft material with a single robot, cf. Fig. 6 left. Here, we generalize our prior work for dual-arm grabbing scenarios. Consider a fixed-base dual-arm robot system grabbing a rigid object with soft deformable pads attached to both end-effectors, cf. Fig. 6 right. We utilize the indexes $(_o)$, $(_l)$, $(_r)$ to indicate the object, left and right manipulator, respectively, and chose the notation $(_{l|r})$ for indicating the left *or* right manipulator.

Let us model the interaction with the soft material as a mass-spring-damper system at each end-effector (also known as Kelvin-Voigt model [29]) with the material's constant, finite stiffness $k_{l|r} > 0$ and damping $p_{l|r} > 0 \in \mathbb{R}$. Denote the relative deformation position of both end-effectors as $\mathbf{z}_l \in \mathbb{R}$, $\mathbf{z}_r \in \mathbb{R}$, and the object's relative position as $\mathbf{z}_o \in \mathbb{R}$, as indicated in Fig. 6 right. Based on Newton's laws, we derive the three equations of motion

$$\mathbf{m}_l\ddot{\mathbf{z}}_l = -\mathbf{f}_l + \underbrace{k_l\left(\mathbf{z}_o - \mathbf{z}_l\right)}_{=\mathbf{f}_{\text{spring-left}}} + \underbrace{p_l\left(\dot{\mathbf{z}}_o - \dot{\mathbf{z}}_l\right)}_{=\mathbf{f}_{\text{damper-left}}}, \tag{9}$$

$$\mathbf{m}_r\ddot{\mathbf{z}}_r = -\underbrace{k_r\left(\mathbf{z}_r - \mathbf{z}_o\right)}_{=\mathbf{f}_{\text{spring-right}}} - \underbrace{p_r\left(\dot{\mathbf{z}}_r - \dot{\mathbf{z}}_o\right)}_{=\mathbf{f}_{\text{damper-right}}} + \mathbf{f}_r, \tag{10}$$

$$\begin{aligned}\mathbf{m}_o\ddot{\mathbf{z}}_o = &-\underbrace{k_l\left(\mathbf{z}_o - \mathbf{z}_l\right)}_{=\mathbf{f}_{\text{spring-left}}} - \underbrace{p_l\left(\dot{\mathbf{z}}_o - \dot{\mathbf{z}}_l\right)}_{=\mathbf{f}_{\text{damper-left}}} \\ &+ \underbrace{k_r\left(\mathbf{z}_r - \mathbf{z}_o\right)}_{=\mathbf{f}_{\text{spring-right}}} + \underbrace{p_r\left(\dot{\mathbf{z}}_r - \dot{\mathbf{z}}_o\right)}_{=\mathbf{f}_{\text{damper-right}}},\end{aligned} \tag{11}$$

with effective mass $\mathbf{m}_{l|r} = \left(\mathbf{o}_1^T\mathbf{J}_{l|r}\mathbf{M}_{l|r}^{-1}\mathbf{J}_{l|r}^T\mathbf{o}_1\right)^{-1} > 0$ [30] and with $\mathbf{f}_{l|r}$ as a function of the applied joint torques $\boldsymbol{\tau}_{l|r}$ based on (1). These three equations can be gathered as

$$\mathcal{M}\begin{bmatrix}\ddot{\mathbf{z}}_l\\ \ddot{\mathbf{z}}_r\\ \ddot{\mathbf{z}}_o\end{bmatrix} = \mathcal{K}\begin{bmatrix}\mathbf{z}_l\\ \mathbf{z}_r\\ \mathbf{z}_o\end{bmatrix} + \mathcal{P}\begin{bmatrix}\dot{\mathbf{z}}_l\\ \dot{\mathbf{z}}_r\\ \dot{\mathbf{z}}_o\end{bmatrix} + \begin{bmatrix}-\mathbf{f}_l\\ \mathbf{f}_r\\ 0\end{bmatrix}, \tag{12}$$

or,

$$\begin{bmatrix}\ddot{\mathbf{z}}_l\\ \ddot{\mathbf{z}}_r\\ \ddot{\mathbf{z}}_o\end{bmatrix} = \mathcal{M}^{-1}\mathcal{K}\begin{bmatrix}\mathbf{z}_l\\ \mathbf{z}_r\\ \mathbf{z}_o\end{bmatrix} + \mathcal{M}^{-1}\mathcal{P}\begin{bmatrix}\dot{\mathbf{z}}_l\\ \dot{\mathbf{z}}_r\\ \dot{\mathbf{z}}_o\end{bmatrix} + \mathcal{M}^{-1}\begin{bmatrix}-\mathbf{f}_l\\ \mathbf{f}_r\\ 0\end{bmatrix} \tag{13}$$

with

$$\mathcal{M} = \begin{bmatrix}\mathbf{m}_l & 0 & 0\\ 0 & \mathbf{m}_r & 0\\ 0 & 0 & \mathbf{m}_o\end{bmatrix},\ \mathcal{M}^{-1} = \begin{bmatrix}\frac{1}{\mathbf{m}_l} & 0 & 0\\ 0 & \frac{1}{\mathbf{m}_r} & 0\\ 0 & 0 & \frac{1}{\mathbf{m}_o}\end{bmatrix} \in \mathbb{R}^{3\times3} \tag{14}$$

and

$$\mathcal{K} = \begin{bmatrix}-k_l & 0 & k_l\\ 0 & -k_r & k_r\\ k_l & k_r & (-k_l-k_r)\end{bmatrix},\ \mathcal{P} = \begin{bmatrix}-p_l & 0 & p_l\\ 0 & -p_r & p_r\\ p_l & p_r & (-p_l-p_r)\end{bmatrix}. \tag{15}$$

Let us introduce the deformation-dependent system state

$$\mathbf{s} = [\mathbf{z}_l^T, \mathbf{z}_r^T, \mathbf{z}_o^T, \dot{\mathbf{z}}_l^T, \dot{\mathbf{z}}_r^T, \dot{\mathbf{z}}_o^T]^T \in \mathbb{R}^6 \tag{16}$$

and the control input

$$\mathbf{u} = \begin{bmatrix}-\frac{1}{\mathbf{m}_l}\mathbf{f}_l\\ \frac{1}{\mathbf{m}_r}\mathbf{f}_r\end{bmatrix} \in \mathbb{R}^2. \tag{17}$$

Reformulating the second-order differential equation (13) yields the continuous-time state-space representation

$$\dot{\mathbf{s}} = \mathbf{A}_c\mathbf{s} + \mathbf{B}_c\mathbf{u} \tag{18}$$

with

$$\mathbf{A}_c = \begin{bmatrix}\mathbf{0}_{3\times3} & \mathbf{I}_{3\times3}\\ \mathcal{M}^{-1}\mathcal{K} & \mathcal{M}^{-1}\mathcal{P}\end{bmatrix} \in \mathbb{R}^{6\times6},\quad \mathbf{B}_c = \begin{bmatrix}\mathbf{0}_{3\times2}\\ \mathbf{I}_{2\times2}\\ \mathbf{0}_{1\times2}\end{bmatrix} \in \mathbb{R}^{6\times2}. \tag{19}$$

We assume small changes in the robot configuration due to relatively small indentations, implying constant inertia $\mathbf{M}$, constant Jacobian $\mathbf{J}$, zero Jacobian derivative $\dot{\mathbf{J}}$. Accordingly, there is a negligible change in the effective masses $\mathbf{m}_{l|r}$ and in the mass matrix $\mathcal{M}$, resulting in constant $\mathbf{A}_c$. Discretization of (18) yields the discrete-time state-space representation with $\mathbf{A}_d \in \mathbb{R}^{6\times6}$, $\mathbf{B}_d \in \mathbb{R}^{6\times2}$, where subscript i denotes steps at time $t = i\Delta t$ utilizing the sample time Δt

$$\mathbf{s}_{i+1} = \mathbf{A}_d\mathbf{s}_i + \mathbf{B}_d\mathbf{u}_i. \tag{20}$$

Note that the resulting discretized acceleration $\ddot{\mathbf{z}}_i$ is linear in terms of state $\mathbf{s}_i$ and control input $\mathbf{u}_i$. Refer to appendix -A for the derivation of matrices $\mathbf{C}$ and $\mathbf{D}$

$$\ddot{\mathbf{z}}_i = \mathbf{C}\mathbf{s}_i + \mathbf{D}\mathbf{u}_i. \tag{21}$$

We can also predict the future forces imposed by the deformed left and right end-effector pads through

$$\mathbf{f}_i = \begin{bmatrix}1 & 0 & 0\\ 0 & 1 & 0\end{bmatrix}\begin{bmatrix}\mathcal{K} & \mathcal{P}\end{bmatrix}\mathbf{s}_i. \tag{22}$$

This *unbounded deformation dynamics* model described so far in (20) is parameterized by the object mass $\mathbf{m}_o$, the configuration-dependent effective masses $\mathbf{m}_{l|r}$, and the soft material properties $k_{l|r}$, $p_{l|r}$. In reality, however, the system behavior is *bounded*. The actual contact-space bounds correlate with the particular penetrating robot hardware limits specified in high-dimensional configuration-space. The previous section showed how to map the structural hardware limits onto contact-space bounds for a single manipulator, which applies here identically for both robot arms. Due to these constraints, not all possible deformation trajectories (i.e., acceleration profiles) are physically achievable with particular robot hardware, which is an often-ignored fact for dynamic deformation control.

Given an initial grabbing deformation state $\mathbf{s}_1$, and a series of future control inputs $\mathbf{u}_1, \mathbf{u}_2, \ldots$ we can now predict the following deformation states $\mathbf{s}_2, \mathbf{s}_3, \ldots$ via (20). Indirectly, we are

also obtaining the predicted accelerations $\ddot{\mathbf{z}}_1, \ddot{\mathbf{z}}_2, \ldots$ via (21), and the contact forces $\mathbf{f}_1, \mathbf{f}_2, \ldots$ via (22). We can then confirm with (7) if this particular series of control inputs results in feasible deformation states that correspond to feasible robot states. Accordingly, knowledge of the *bounded deformation dynamics* is of utmost importance for the constrained model-preview proposed in the following.

B. Impact-Aware Model Predictive Control

Always considering that the contacts will happen right after the current control cycle, we formulate an optimization problem that plans a feasible dual-arm penetration trajectory in the contact-space over a preview horizon of h steps, starting from the exact moment of the contact transition with $\mathbf{z}_{1_l} = \mathbf{z}_{1_r} = \mathbf{z}_{1_o} = 0$ and $\dot{\mathbf{z}}_{1_o} = 0$. The decision variables consist of the initial pre-impact velocities $\dot{\mathbf{z}}_{1_l}, \dot{\mathbf{z}}_{1_r}$, which are to be optimized, and the subsequent control inputs $\mathbf{u}_1, \ldots, \mathbf{u}_h$. We propose the linear problem:

$$
\begin{aligned}
\min_{\dot{\mathbf{z}}_{1_l}, \dot{\mathbf{z}}_{1_r}, \mathbf{u}_1^T, \ldots, \mathbf{u}_h^T} \quad & \dot{\mathbf{z}}_{1_r} - \dot{\mathbf{z}}_{1_l} \qquad (23)\\
\text{subject to} \quad & \mathbf{s}_1 = \begin{bmatrix} \mathbf{0} \\ \dot{\mathbf{z}}_1 \end{bmatrix}, \ \mathbf{s}_i = \begin{bmatrix} \mathbf{z}_i \\ \dot{\mathbf{z}}_i \end{bmatrix} \\
& \mathbf{s}_{i+1} = \mathbf{A}_d \mathbf{s}_i + \mathbf{B}_d \mathbf{u}_i \\
& \dot{\mathbf{z}}_{1_o} = \mathbf{0} \text{ and } \dot{\mathbf{z}}_{h_{l|r}} = \mathbf{0} \\
& \underline{\mathbf{z}} \leq \mathbf{z}_i = [\mathbf{I}, \ \mathbf{0}]\, \mathbf{s}_i \leq \bar{\mathbf{z}} \\
& \underline{\dot{\mathbf{z}}} \leq \dot{\mathbf{z}}_i = [\mathbf{0}, \ \mathbf{I}]\, \mathbf{s}_i \leq \bar{\dot{\mathbf{z}}} \\
& \underline{\mathbf{p}} \leq \mathbf{P}_{\ddot{\mathbf{z}}}\, \ddot{\mathbf{z}}_i + \mathbf{P}_{\mathbf{f}}\, \mathbf{f}_i \leq \bar{\mathbf{p}}
\end{aligned}
$$

This contact-space MPC problem can be solved efficiently in each control cycle and requires $k_{l|r}$, $p_{l|r}$, $\mathbf{m}_{l|r}$, $\mathbf{m}_o$ and h.

The upper and lower bounds on $\mathbf{z}$ enforce the penetration and ensure that the minimization of $\dot{\mathbf{z}}_{1_r} - \dot{\mathbf{z}}_{1_l}$ is unique[4]. However, due to the linear objective to be optimized, a set of infinite trajectories may exist that are all optimal. In order to select a unique series of control inputs $\mathbf{u}_1, \ldots, \mathbf{u}_h$, a secondary low-weight prioritized quadratic objective may be added to the optimization problem. For example, in Fig. 8, we minimize the quadratic error between desired and predicted forces in the nullspace of the primary objective. Note that this does not affect the maximum impact velocities.

In practice, we recompute (23) in each control cycle. We are interested only in the optimized pre-impact velocities $\dot{\mathbf{z}}_{1_l}, \dot{\mathbf{z}}_{1_r}$, which are tracked with velocity controllers by the end-effectors. Consequently, this control scheme does not require knowledge of the contact location and the box width, as it operates the manipulators within the feasible impact limits that are updated in each control cycle.

Note that this control scheme does not distinguish whether the soft material is attached to the end-effectors or to the object. Consequently, the proposed approach also generalizes to swiftly grabbing soft objects with rigid end-effectors.

[4]In Fig. 6 right, the left arm is constrained by $\mathbf{z}_l = 0$ and the right arm by $\bar{\mathbf{z}}_r = 0$. Consequently, $\dot{\mathbf{z}}_{1_l} > 0$ and $\dot{\mathbf{z}}_{1_r} < 0$ is enforced.

C. Asynchronous Contact Transitions

Encountering asynchronous contact transitions with a delay of few iterations is not surprising, since we do not explicitly plan the contact time and roughly assume the object is placed approximately in the center of the two end-effectors. We observe these two contact events by monitoring the end-effector forces, either via wrist-mounted sensors or via external joint torque measurements mapped onto the end-effector. For example, after making contact with the right (resp. left) soft pad, the object could start moving to the left (resp. right) while compressing the right (resp. left) pad. Inferring the objects relative position and velocity as well as the compression is straightforward given the known model of the pad and the measured force. The MPC (23) is then initialized with the systems current state, continuing to assume the other contact event to occur after the current control cycle, etc. Hence, the above formulation is slightly adapted with $\mathbf{z}_{1_r} \neq 0$, $\mathbf{z}_{1_l} = 0$ (resp. $\mathbf{z}_{1_r} = 0$, $\mathbf{z}_{1_l} \neq 0$) and with $\mathbf{z}_{1_o} \neq 0$, $\dot{\mathbf{z}}_{1_o} \neq 0$ according to the measurements. The MPC formulation automatically accounts for the worst case and computes an optimum contact velocity for the left (resp. right) end-effector that is tracked. Now, if the second contact event is not detected after few iterations, the controller switches to the handling recovery procedure for such cases.

D. Comparison with Prior Work and Discussion

Our prior work [9], models the system dynamics for a single-arm soft poking scenario, cf. Fig. 6 left. Note that the dual-arm model proposed in this paper (cf. Fig. 6 right) is more general. This is easy to see in (18) when treating the object and the right manipulator (with zero joints) as part of the rigid environment. Basically, there are no equations of motion for the rigid environment. We obtain the single-arm model described in [9], with $\mathcal{K} = -k \in \mathbb{R}$, $\mathcal{P} = -p \in \mathbb{R}$, $\mathcal{M} = \mathbf{m} \in \mathbb{R}$, $\mathbf{s} = [\mathbf{z}, \dot{\mathbf{z}}]^T \in \mathbb{R}^2$, $\mathbf{u} = -\frac{1}{\mathbf{m}}\mathbf{f} \in \mathbb{R}$, resulting in

$$
\mathbf{A}_c = \begin{bmatrix} \mathbf{0}_{1\times1} & \mathbf{I}_{1\times1} \\ \mathcal{M}^{-1}\mathcal{K} & \mathcal{M}^{-1}\mathcal{P} \end{bmatrix} \in \mathbb{R}^{2\times2}, \quad \mathbf{B}_c = \begin{bmatrix} \mathbf{0}_{1\times1} \\ \mathbf{I}_{1\times1} \end{bmatrix} \in \mathbb{R}^{2\times1}. \quad (24)
$$

Note that the proposed approach can seamlessly control a heterogeneous dual-arm plattform, consisting of manipulators from two different manufacturers. Applying instead the single-arm method [9] independently for each arm would either cause grabbing failures or result in more conservative behavior. Such a naive approach is missing the fact that the object may swing between the two end-effectors. This aspect becomes relevant when operating robot arms with different kinematic/dynamic properties, resulting in different contact velocities and different effective masses for both end-effectors. Moreover, the benefits of having a centralized multi-robot control w.r.t a controller per arm, is thoroughly explained in [31].

V. Real-Robot Experiment

The experimental platform is a dual-arm setup composed of two Panda manipulators from FrankaEmika with each 7 DOF, utilizing 3D-printed plastic end-effectors equipped with two identical soft pads (0.1 m $\times$ 0.1 m contact surface and 0.05 m depth). The dual-robot platform is controlled based

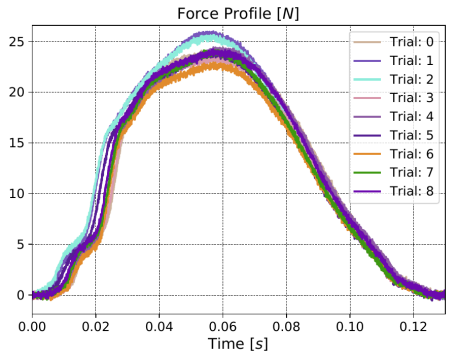

Fig. 7: Recorded data of nine impacts with the Panda. The end-effector soft-pad moves horizontally with 0.18 m/s, bumps orthogonally into a force sensor mounted to a wall, and pulls back upon contact detection.

on our existing multi-objective QP-control framework [31]. We implemented a new extension (available open-source[5]) to synchronize the two Panda manipulators, a feature that the manufacturer does not officially support. Our experiments are made according to representative objects and simplified scenarios provided by industrial use-cases.

In a preliminary study, we evaluated the contact force profile for the chosen soft pad. Therefore, a single panda robot repeatedly impacts an ATI-mini45 force-torque sensor with an end-effector velocity of 0.18 m/s, showing consistent behavior in Fig. 7. The force sensor data is acquired with a frequency of 25 kHz, that is sufficient enough to capture such impact dynamics. The overall impact lasts 0.13 s, and the maximum force is about 25 N. The soft impact is considerably longer and significantly less forceful than our similar experiments with a rigid end-effector, see data in [32].

We identified the model parameters of the soft material offline with the procedure described in [9], [17]. Employing the `stabiliplus` library[6], (5) is solved in every control cycle. The optimization problem (23) is parameterized with $h = 15$ steps and the discretization sample time $\Delta t = 25$ ms, resulting in the preview horizon of 0.375 s. We solve it utilizing the `COPRA` library[7]. The optimization result constitutes an upper bound on the pre-impact velocities and should be as up-to-date as possible. Primary end-effector velocity tasks track the maximum possible pre-impact velocities with both manipulators. Besides, secondary tasks minimize the joint accelerations to account for the redundancy, thereby avoiding elbow self-motion to maintain the effective masses. The controller switches to an admittance task [31] upon contact detection. The admittance controller incorporates the robot's force sensor signals, thereby accounting for material model inaccuracies. It tracks the reference force 60 N (depending on the object's mass) more accurately in practice than following the previously planned deformation trajectory. More research is needed to include the actual force measurements into the state-space representation for the MPC (18).

We here discuss only one object experiment due to space limitations – please refer to the video for the other objects. The box to be grabbed weights 4 kg, is 0.38 m wide (not known by the controller), and is placed initially in the center between the two end-effectors[8]. Analyzing the logged data, all hardware limits are satisfied. After moving 0.24 m within 0.12 s, the end-effectors detect the contact with a relative pre-impact velocity of ± 0.61 m/s, refer to Fig. 8. The box lift-up motion is triggered upon ending both contact phases. Steady-state force-tracking is reached after approximately 0.3 s of deformation and partial restitution, confirming the chosen preview duration. The final measured force is close to the reference force; Fig. 8 also shows the planned deformation trajectory at the contact event. As discussed above, this prediction is not necessarily unique because the linear program (23) may yield an infinite set of solutions in terms of different sequences of control inputs.

VI. Conclusion and Future Work

Intentionally generated impacts accelerate contact transitions and speed-up the manipulation of objects by collaborative multi-robot teams in industrial automation sorting processes. Equipping the robot end-effector tips with deformable soft pads extends the system's motion capabilities, allowing larger impact velocities. Utilizing the deformable contact force model, we plan (at runtime) and execute constrained deformation trajectories for powerful intentional impact-aware grabbing: Our approach to bi-manual object manipulation swiftly grabs and lifts bulky box objects without compromising the robot's structural hardware limitations.

Extension to multi-arm systems [33] requires to adapt grasp quality measures proposed for rigid contacts [34] to deformable contacts. Future work will tackle the planning of pre-impact null-space postures, influencing the end-effector's effective mass [30]. We are also interested in swiftly grabbing moving objects that would require considering friction and tangential relative motions. Finally we are also investigating other possible soft materials.

Appendix

A. Deformation acceleration $\ddot{\mathbf{z}}_i$ reformulated w.r.t. $\mathbf{s}_i$ and $\mathbf{u}_i$

Let us denote the matrix elements of matrices $\mathbf{A}_d, \mathbf{B}_d$ as

$$\mathbf{A}_d = \begin{bmatrix} \mathcal{A}_{1:3,1:3} & \mathcal{A}_{1:3,4:6} \\ \mathcal{A}_{4:6,1:3} & \mathcal{A}_{4:6,4:6} \end{bmatrix} \text{ and } \mathbf{B}_d = \begin{bmatrix} \mathcal{B}_{1:3,1:2} \\ \mathcal{B}_{4:6,1:2} \end{bmatrix}$$

Reformulate (20) with $\mathbf{z} = [\mathbf{z}_l^T, \mathbf{z}_r^T, \mathbf{z}_o^T]^T$, $\dot{\mathbf{z}} = [\dot{\mathbf{z}}_l^T, \dot{\mathbf{z}}_r^T, \dot{\mathbf{z}}_o^T]^T$

$$\dot{\mathbf{z}}_{i+1} = \left[\mathcal{A}_{4:6,1:3}\right] \mathbf{z}_i + \left[\mathcal{A}_{4:6,4:6}\right] \dot{\mathbf{z}}_i + \left[\mathcal{B}_{4:6,1:2}\right] \mathbf{u}_i$$

The acceleration $\ddot{\mathbf{z}}_i$ is linear in terms of deformation state $\mathbf{s}_i$ and control input $\mathbf{u}_i$

$$\begin{aligned} \ddot{\mathbf{z}}_i &= \frac{1}{\Delta t}\left(\dot{\mathbf{z}}_{i+1} - \dot{\mathbf{z}}_i\right) \\ &= \frac{1}{\Delta t}\left[\left[\mathcal{A}_{4:6,1:3}\right] \mathbf{z}_i + \left(\left[\mathcal{A}_{4:6,4:6}\right] - \mathbf{I}\right) \dot{\mathbf{z}}_i + \left[\mathcal{B}_{4:6,1:2}\right] \mathbf{u}_i\right] \\ &= \frac{1}{\Delta t}\left[\left[\mathcal{A}_{4:6,1:3}\right], \left(\left[\mathcal{A}_{4:6,4:6}\right] - \mathbf{I}\right)\right] \begin{bmatrix} \mathbf{z}_i \\ \dot{\mathbf{z}}_i \end{bmatrix} + \frac{1}{\Delta t}\left[\mathcal{B}_{4:6,1:2}\right] \mathbf{u}_i \\ &= \mathbf{C}\mathbf{s}_i + \mathbf{D}\mathbf{u}_i \end{aligned}$$

[5]See https://github.com/jrl-umi3218/mc_franka
[6]See https://github.com/JulienRo7/stabiliplus
[7]See https://github.com/jrl-umi3218/copra

[8]Object dynamics and friction coefficient are only required for selecting the minimum needed reference squeezing force. The object width can be inferred upon contact detection.

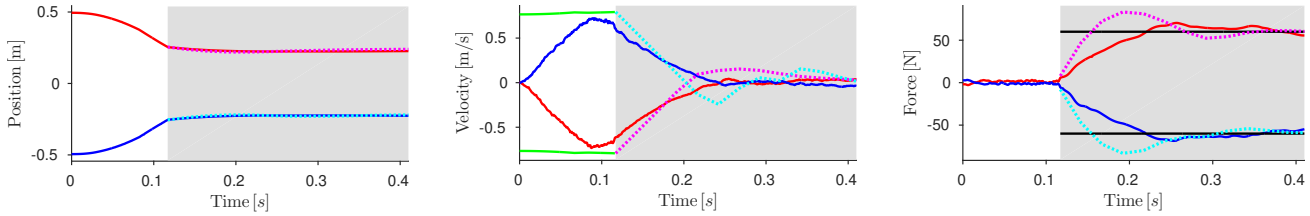

Fig. 8: Impact-aware bi-manually grabbing a 4 kg box with maximum configuration-dependent contact velocities ± 0.61 m/s. The absolute measurements along the contact normal are indicated by solid red and blue lines for the two manipulators. Planned trajectories for the deformation phase (shaded area) are plotted as dotted purple and cyan lines when detecting the contact at 0.12 s. The green curve shows the maximum feasible pre-impact velocity at a given time step that is tracked (before making contact) and black the reference contact force of 60 N (after making contact).

Accordingly, we can reformulate (6) in terms of deformation state $\mathbf{s}_i$ and control input $\mathbf{u}_i$ by substituting (22)

$$\mathbf{P}\begin{bmatrix}\ddot{\mathbf{z}}_i\\ \mathbf{f}_i\end{bmatrix}=\mathbf{P}\begin{bmatrix}\mathbf{C}\mathbf{s}_i+\mathbf{D}\mathbf{u}_i\\ [\mathcal{K},\mathcal{P}]\,\mathbf{s}_i\end{bmatrix}=\mathbf{P}\begin{bmatrix}\mathbf{C}\\ [\mathcal{K},\mathcal{P}]\end{bmatrix}\mathbf{s}_i+\mathbf{P}\begin{bmatrix}\mathbf{D}\\ \mathbf{0}\end{bmatrix}\mathbf{u}_i$$

ACKNOWLEDGMENT

The authors thank Dr. Pierre Gergondet for his support and Julien Roux for providing a C++ implementation of [28].

REFERENCES

[1] S. Hayati, "Hybrid position/force control of multi-arm cooperating robots," in *IEEE Int. Conf. on Robotics and Automation*, vol. 3, 1986, pp. 82–89.
[2] S. Lee, "Dual redundant arm configuration optimization with task-oriented dual arm manipulability," *IEEE Transactions on Robotics and Automation*, vol. 5, no. 1, pp. 78–97, 1989.
[3] N. Dehio, J. Smith, D. L. Wigand, G. Xin, H.-C. Lin, J. J. Steil, and M. Mistry, "Modeling and Control of Multi-Arm and Multi-Leg Robots: Compensating for Object Dynamics during Grasping," in *IEEE Int. Conf. on Robotics and Automation*, 2018, pp. 294–301.
[4] B. Henze, M. A. Roa, and C. Ott, "Passivity-based whole-body balancing for torque-controlled humanoid robots in multi-contact scenarios," *Int. Journal of Robotics Research*, vol. 35, no. 12, pp. 1522–1543, 2016.
[5] H. Arisumi, J.-R. Chardonnet, A. Kheddar, and K. Yokoi, "Dynamic lifting motion of humanoid robots," in *IEEE Int. Conf. on Robotics and Automation*, 10-14 April 2007, pp. 2661–2667.
[6] T. B. Sheridan, "Three models of preview control," *IEEE Transactions on Human Factors in Electronics*, vol. HFE-7, no. 2, pp. 91–102, 1966.
[7] Y. Nakamura, T. Zhang, and M. Minami, "Multi-preview configuration control for predictive behavior of redundant manipulator," in *ICCAS-SICE*, 2009, pp. 3117–3123.
[8] J. Lee, S. H. Bang, E. Bakolas, and L. Sentis, "Mpc-based hierarchical task space control of underactuated and constrained robots for execution of multiple tasks," in *IEEE Conf. on Decision and Control*, 2020, pp. 5942–5949.
[9] N. Dehio and A. Kheddar, "Robot-safe impacts with soft contacts based on learned deformations," in *IEEE Int. Conf. on Robotics and Automation*, 2021, pp. 1357–1363.
[10] S. Faik and H. Witteman, "Modeling of impact dynamics: A literature survey," in *Int. ADAMS User Conference*, vol. 80, 2000.
[11] S. Pashah, M. Massenzio, and E. Jacquelin, "Prediction of structural response for low velocity impact," *Int. Journal of Impact Engineering*, vol. 35, no. 2, pp. 119–132, 2008.
[12] M. Murooka, R. Ueda, S. Nozawa, Y. Kakiuchi, K. Okada, and M. Inaba, "Global planning of whole-body manipulation by humanoid robot based on transition graph of object motion and contact switching," *Advanced Robotics*, vol. 31, no. 6, pp. 322–340, 2017.
[13] L. Yan, Y. Yang, W. Xu, and S. Vijayakumar, "Dual-arm coordinated motion planning and compliance control for capturing moving objects with large momentum," in *IEEE/RSJ Int. Conf. on Intelligent Robots and Systems*, 2018, pp. 7137–7144.
[14] M. Gienger, D. Ruiken, T. Bates, M. Regaieg, M. Meißner, J. Kober, P. Seiwald, and A.-C. Hildebrandt, "Human-robot cooperative object manipulation with contact changes," in *IEEE Int. Conf. on Intelligent Robots and Systems*, 2018, pp. 1354–1360.
[15] T. Watanabe, "Softness effects on manipulability and grasp stability," in *IEEE Int. Conf. on Intelligent Robots and Systems*, 2011, pp. 1398–1404.
[16] T. Wimböck, C. Ott, A. Albu-Schäffer, and G. Hirzinger, "Comparison of object-level grasp controllers for dynamic dexterous manipulation," *Int. Journal of Robotics Research*, vol. 31, no. 1, pp. 3–23, 2012.
[17] M. Azad, V. Ortenzi, H.-C. Lin, E. Rueckert, and M. Mistry, "Model estimation and control of compliant contact normal force," in *IEEE/RAS Int. Conf. on Humanoid Robots*, 2016, pp. 442–447.
[18] G. Smoljkic, G. Borghesan, D. Reynaerts, J. De Schutter, J. V. Sloten, and E. V. Poorten, "Constraint-based interaction control of robots featuring large compliance and deformation," *IEEE Transactions on Robotics*, vol. 31, no. 5, pp. 1252–1260, 2015.
[19] K. Bouyarmane and A. Kheddar, "FEM-based static posture planning for a humanoid robot on deformable contact support," in *IEEE/RAS Int. Conf. on Humanoid Robots*, 2011, pp. 487–492.
[20] G. De Magistris, A. Pajon, S. Miossec, and A. Kheddar, "Humanoid walking with compliant soles using a deformation estimator," in *IEEE Int. Conf. on Robotics and Automation*, 2016, pp. 1757–1762.
[21] E. Coevoet, A. Escande, and C. Duriez, "Soft robots locomotion and manipulation control using FEM simulation and quadratic programming," in *Int. Conf. on Soft Robotics*, 2019, pp. 739–745.
[22] M. Rijnen, E. de Mooij, S. Traversaro, F. Nori, N. van de Wouw, A. Saccon, and H. Nijmeijer, "Control of humanoid robot motions with impacts: Numerical experiments with reference spreading control," in *IEEE Int. Conf. on Robotics and Automation*, 2017, pp. 4102–4107.
[23] Y. Wang and A. Kheddar, "Impact-friendly robust control design with task-space quadratic optimization," in *Proceedings of Robotics: Science and Systems*, 2019.
[24] Y. Wang, N. Dehio, A. Tanguy, and A. Kheddar, "Impact-aware task-space quadratic-programming control," *arxiv*, 2020. [Online]. Available: https://arxiv.org/abs/2006.01987
[25] V. Samy, S. Caron, K. Bouyarmane, and A. Kheddar, "Post-impact adaptive compliance for humanoid falls using predictive control of a reduced model," in *IEEE-RAS Int. Conf. on Humanoid Robotics*, 2017, pp. 655–660.
[26] R. Orsolino, M. Focchi, S. Caron, G. Raiola, V. Barasuol, D. G. Caldwell, and C. Semini, "Feasible region: An actuation-aware extension of the support region," *IEEE Transactions on Robotics*, vol. 36, no. 4, pp. 1239–1255, 2020.
[27] T. Bretl and S. Lall, "Testing static equilibrium for legged robots," *IEEE Transactions on Robotics*, vol. 24, no. 4, pp. 794–807, 2008.
[28] J. Roux, S. Samadi, E. Kuroiwa, T. Yoshiike, and A. Kheddar, "Control of humanoid in multiple fixed and moving unilateral contacts," in *Int. Conf. on Advanced Robotics*, 2021, pp. 793–799.
[29] W. Flügge, "Viscoelasticity," *Waltham, Mass.:Blaisdell Publishing Company*, 1967.
[30] N. Mansfeld, B. Djellab, J. R. Veuthey, F. Beck, C. Ott, and S. Haddadin, "Improving the performance of biomechanically safe velocity control for redundant robots through reflected mass minimization," in *IEEE/RSJ Int. Conf. on Intelligent Robots and Systems*, 2017, pp. 5390–5397.
[31] K. Bouyarmane, K. Chappellet, J. Vaillant, and A. Kheddar, "Quadratic programming for multirobot and task-space force control," *IEEE Transactions on Robotics*, vol. 35, no. 1, pp. 64–77, 2019.
[32] Y. Wang, N. Dehio, and A. Kheddar, "On inverse inertia matrix and contact-force model for robotic manipulators at normal impacts," *IEEE Robotics and Automation Letters*, vol. 7, no. 2, pp. 3648–3655, 2022.
[33] N. Dehio, J. Smith, D. L. Wigand, P. Mohammadi, M. Mistry, and J. J. Steil, "Enabling impedance-based physical humanmultirobot collaboration: Experiments with four torque-controlled manipulators," *The Int. Journal of Robotics Research*, vol. 41, no. 1, pp. 68–84, 2022.
[34] M. A. Roa and R. Suárez, "Grasp quality measures: review and performance," *Autonomous Robots*, vol. 38, no. 1, pp. 65–88, 2015.